American Mineralogist, Volume 93, pages 821–830, 2008

Interlayer potassium and its neighboring atoms in micas: Crystal-chemical modeling and XANES spectroscopy

Maria Franca Brigatti,[1,*] Daniele Malferrari,[1] Marco Poppi,[1] Annibale Mottana,[2,3] Giannantonio Cibin,[2,3,†] Augusto Marcelli,[3] and Gianfelice Cinque[3,†]

[1]Dipartimento di Scienze della Terra, Università degli Studi di Modena e Reggio Emilia, Via S. Eufemia 19, I-41100 Modena MO, Italy
[2]Dipartimento di Scienze Geologiche, Università degli Studi Roma Tre, Largo S. Leonardo Murialdo 1, I-00146 Roma RM, Italy
[3]Laboratori Nazionali di Frascati, Istituto Nazionale di Fisica Nucleare, Via Enrico Fermi 30, I-00040 Frascati RM, Italy

Abstract

A detailed description of the interlayer site in trioctahedral true micas is presented based on a statistical appraisal of crystal-chemical, structural, and spectroscopic data determined on two sets of trioctahedral micas extensively studied by both X-ray diffraction refinement on single crystals (SC-XRD) and X-ray absorption fine spectroscopy (XAFS) at the potassium *K*-edge. Spectroscopy was carried out on both random powders and oriented cleavage flakes, the latter setting taking advantage of the polarized character of synchrotron radiation. Such an approach (AXANES) is shown to be complementary to crystal-chemical investigation based on SC-XRD refinement. However, the results are not definitive as they focus on few samples having extreme features only (e.g., end-members, unusual compositions, and samples with extreme and well-identified substitution mechanisms). The experimental absorption *K*-edge (XANES) for potassium was decomposed by calculation and extrapolated into a full in-plane absorption component ($\sigma_{\parallel}$) and a full out-of-plane absorption component ($\sigma_{\perp}$). These two patterns reflect different structural features: $\sigma_{\parallel}$ represents the arrangement of the atoms located in the mica interlayer space and facing tetrahedral sheets; $\sigma_{\perp}$ is associated with multiple-scattering interactions entering deep into the mica structure, thus also reflecting interactions with the heavy atoms (essentially Fe) located in the octahedral sheet. The out-of-plane patterns also provide insights into the electronic properties of the octahedral cations, such as their oxidation states (e.g., Fe^{2+} and Fe^{3+}) and their ordering (e.g., *trans*- vs. *cis*-setting). It is also possible to distinguish between F- and OH-rich micas due to peculiar absorption features originating from the F vs. OH occupancy of the O4 octahedral site. Thus, combining crystal-chemical, structural, and spectroscopic information is shown to be a practical method that allows, on one hand, assignment of the observed spectroscopic features to precise structural pathways followed by the photoelectron within the mica structure and, on the other hand, clarification of the amount of electronic interactions and forces acting onto the individual atoms at the various structural sites.

Keywords: Crystal structure, X-ray absorption spectroscopy, XAFS, XRD, correlation, assignment

Introduction

Crystal chemistry and topology of the interlayer cations in micas have been detailed by several authors and readily appeared not only to be sensitive to interlayer composition, but also to mirror the topology of other sites occurring in the mica structure (i.e., tetrahedral, octahedral, and anionic sites). Pauling (1930), in the model describing the idealized and undeformed mica structure, assumed a coordination number of twelve for the interlayer cation (A), which bonds O atoms on two facing tetrahedral sheets (i.e., six tetrahedral basal O atoms on each sheet at the same distance). As a consequence, the O atoms surrounding the interlayer cation had $P(6/m)mm$ symmetry. Later on, an alternative, more appropriate ditrigonal model was suggested (Belov 1949; Radoslovich 1961; Radoslovich and Norrish 1962). According to this model, the interlayer cation has six closest O atoms as nearest neighbors and six other more distant O next-nearest neighbors; thus the coordination becomes ditrigonal, with the O atoms surrounding the interlayer cation (A) arranged in two different configurations having $P\bar{3}1m$ and $P\bar{3}2m$ symmetry, respectively (Smyth and Bish 1988).

Weiss et al. (1992) determined the effective coordination number, ECoN (i.e., the number of neighboring anions around a cation that are actually linked to it by bonds of nearly equal length and force; Hoppe 1979) of the interlayer A cation in micas. ECoN was found to be affected by the stacking of the layers and by the interlayer separation, which reflects cation and anion substitutions in octahedral sites (Brigatti and Guggenheim 2002), and to vary smoothly and continuously from 12 to 6 as a function of the in-plane rotation of the adjacent tetrahedra. Even

* E-mail: brigatti@unimore.it
† Present address: Diamond Light Source, Rutherford Appleton Laboratory, Chilton, Didcot, Oxfordshire OX11 0QX, U.K.

in micas where K is by far the main A cation, ECoN shows a large variation. It is close to 12 in tainiolite and annite, it varies from 11 to 9 in polylithionite, ferroan polylithionite, phlogopite, and ferroan phlogopite, and it decreases even more in muscovite (8–9), probably because of the different size of M1 (vacant cavity) and M2 (mostly Al-occupied) octahedral sites. In all micas, ECoN was found to correlate well with the in-plane tetrahedral rotation angle (parameter α: Takéuchi and Sadanaga 1959).

The relationships between the interlayer cation and its surrounding O atoms were also found to be associated with other distortions (Brigatti and Guggenheim 2002), both of the individual tetrahedra and of the whole tetrahedral sheet (parameters τ and Δz). In an ideal tetrahedron, the flattening angle τ, defined as the average of O_{apical}-T-O_{basal} angles ($\tau = \Sigma_{i=1}^{3}(O_{apical}\text{-T-}O_{basal})_i/3$), is equal to arcos(–1/3) ≅ 109.47°. In real mica structures, the τ value can deviate from its ideal value as a function of the relative position along **c*** for the basal O atoms with respect both to the tetrahedral cation and to the mean basal-edge length and the mean tetrahedral-edge value. These shifts cause a variation in the electrostatic energy associated with the tetrahedral cation to basal O atom distance, which is compensated by a variation in the repulsion between the interlayer and tetrahedral cations (Brigatti and Guggenheim 2002). Finally, the basal O atom plane corrugation effect (Δz; Lee and Guggenheim 1981) must be considered, which reflects differences in distance between apical O atoms linked to octahedra of different size. Δz is limited in trioctahedral micas, where the M1 *cis*-octahedral site is about as great as the M2 = M3 *trans*-octahedral sites, and increases in Li-rich micas, which have M1 ≅ M3 > M2 (or M1 ≅ M2 > M3).

For all these reasons, variations observed in the topology of the interlayer site for K-rich trioctahedral micas were always attributed to external constraints, such as the adjustment of topological changes affecting other structural sites, rather than to interlayer chemical substitutions and the ensuing changes in bond energy. However, this attribution should be tested. A chemically specific spectroscopic method such as X-ray absorption near-edge spectroscopy (XANES) at the *K*-edge may contribute to a better characterization of the topology of the interlayer site, as well as of all the other structural sites affecting this latter site, albeit indirectly. Consequently, Cibin et al. (2005) studied the potassium *K*-edge XANES to characterize better the local structure and order of this cation, which is dominant in true micas. They examined powdered trioctahedral mica samples with different tetrahedral and octahedral compositions, and found that XANES features reflect both cation coordination and the contributions of tetrahedral as well as octahedral cations acting upon the interlayer.

The potassium *K*-edge spectra of trioctahedral micas show five discernible features in the energy range 3600–3650 eV that is usually assumed to be the XANES region at this energy for this type of compound (Bianconi 1988; Mottana 2004). Two or three other weak features follow up to 3700 eV; these are within the energy range that recent computer codes based on the MS theory can satisfactorily explain and reproduce (Benfatto and Della Longa 2001; Benfatto et al. 2001; Natoli et al. 2003). They can also preferentially be explained and fitted on the basis of the single-scattering (SS) theory using EXAFS (Stern and Heald 1983; Galoisy 2004).

Spectra in the 3625–3650 eV energy range that comprise the intermediate multiple-scattering (IMS) region (Natoli and Benfatto 1986) of all micas are nearly identical in shape, although displaying some shifts in energy, as do the higher-energy regions extending to the EXAFS region. The constant shape of these spectral regions was interpreted as proof of the isostructural character of all members of simple solid-solution series (e.g., Mottana et al. 2002). This conclusion also holds true for much more complex groups of compounds such as the micas, which undergo numerous chemically driven structural rearrangements (i.e., they are not isotypic, but homeotypic compounds). Conversely, this evidence may also be confidently taken to reflect the fact that the local structure around the K^+ cation is practically the same for all interlayers, regardless of whether the mica octahedral sheet is tri- or di-octahedral. Alternatively, it might also be explained by suggesting that the photoelectron outgoing from the potassium absorber does not cross the barrier represented by the O and OH anions located on the outer tetrahedral and octahedral planes and that photo-electron pathways are restricted to the interlayer only (i.e., they are in-plane). In such a case, numerous features observed in the experimental potassium *K*-edge spectra of micas could be interpreted, alternatively, as focusing effects against distant potassium atoms all along the interlayer (Kuzmin and Parent 1994). In the full multiple-scattering (FMS) energy range (3605–3625 eV; Natoli and Benfatto 1986), the XANES features do not only arise from contributions that essentially depend upon the local atomic structural arrangement around the potassium absorber (i.e., bond length and orientation in the first and second coordination sphere) but include also long range multiple-scattering contributions. They also contain an important component arising from electronic contributions to the K^+ cation that result from its interactions with the anions directly surrounding it, as would be related to bond strength. In this sub-region of the spectra, there is evidence of systematic changes.

However, micas are phyllosilicates, with the whole crystal structure made of overlapping layers that are similar to one another. Thus, their XANES spectra should be affected by the polarization direction of the incident polarized beam of synchrotron radiation onto the layer structure. For this reason, in a more advanced work, Cibin et al. (2006) applied angle-dependent X-ray absorption spectroscopy (AXAS; Brouder 1990; Brouder et al. 1990) to study potassium coordination in K-rich trioctahedral micas. They found that the in-plane absorption component pattern (i.e., the spectrum calculated back to exactly the 0° angle θ of the electric vector of the incident synchrotron radiation beam) reflects the arrangement of the atoms located in the mica interlayer space and facing tetrahedral sheets. The out-of-plane component pattern (i.e., the spectrum extrapolated to $\theta = 90°$ from the previous plane) reflects multiple-scattering interactions of potassium entering deep into the mica structure, beyond the tetrahedral sheet and well into the octahedral sheet.

In this work we aim to match crystal-chemical and structural data derived from a detailed description of the mica topological variations obtained in a large SC-XRD refinement data set with XANES and AXANES data obtained on the same mica samples. The purpose of our investigation is to describe better the local environment of the potassium atom in the mica structure and the constraints imposed by the layer structure onto its coordination,

so as to univocally relate the variation of the observed XANES features with well-defined structural parameters determined on the micas.

DATABASE

The aim of this work, as previously stated, is to use a statistical approach (via SPSS-15.0 Statistical Analyses Package) to relate XANES spectral features to a large number of chemical and structural parameters, projected on different crystallographic planes, and calculated starting from unit-cell parameters and atomic coordinates. To this purpose we used structural and spectroscopic data that we obtained in the recent past and published elsewhere (Brigatti and Poppi 1993; Alietti et al. 1995; Brigatti et al. 1996, 1998, 1999, 2000; Tombolini et al. 2002a; Cibin et al. 2005, 2006; Schingaro et al. 2005; Marcelli et al. 2006). They all can be retrieved from our data bank together those not yet available in print, which are available from M.F.B. upon request. The experimental conditions and methods used, either in recording and fitting the XAFS data or in refining the structures by SC-XRD, can be found in the literature just cited.

The data set under study here comprises 16 trioctahedral micas, all from 1*M* polytype, and can be chemically divided in three subsets on the basis of crystal-chemical data (Table 1[1]). The first and largest subset comprises 10 samples falling predominantly along the phlogopite-annite join (*C*2/*m* symmetry); the second subset includes two tetra-ferriphlogopite samples with a very substantial amount of tetrahedral ferric iron (*C*2/*m* symmetry); and the third subset contains four Li-rich micas (*C*2 symmetry). Some samples larger in size were used for AXANES experiments, whereas others, smaller in size, were analyzed only via powder XANES experiments.

Schematics of the mica interlayer structure with the positions taken by the atoms nearest and next-nearest to the A cation in the tetrahedral and octahedral sheets are presented in Figures 1a and 1b for *C*2/*m* and *C*2 symmetry, respectively. Spectroscopic features and main structural parameters, with focus for the ones characterizing interlayer site topology as seen in Figure 1, are listed in Tables 2 and 3. Some representative XANES spectra are reported in Figure 2. The mathematical derivation and definitions for a selected number of parameters are reported in the appendix[1].

XANES powder spectra

XANES power data discussed in this work refer to a sub-set of 13 trioctahedral micas (Table 2): ten are micas spanning in composition from phlogopite to annite, two are tetra-ferriphlogopites and one is a Li-siderophyllite (Table 1[1]). Some selected spectra are also reported in Figure 2a, where features, previously discussed, are labeled from A to E. XANES powder spectra were

[1]Deposit item AM-08-022, Table 1 and appendix (the mathematical derivation and definitions for a selected number of parameters). Deposit items are available two ways: For a paper copy contact the Business Office of the Mineralogical Society of America (see inside front cover of recent issue) for price information. For an electronic copy visit the MSA web site at http://www.minsocam.org, go to the American Mineralogist Contents, find the table of contents for the specific volume/issue wanted, and then click on the deposit link there.

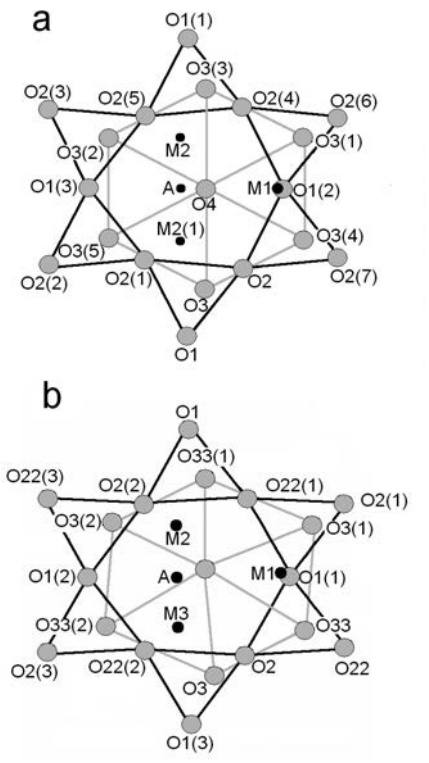

FIGURE 1. Interlayer A cation and its neighboring atoms for the *C*2/*m* (**a**) and *C*2 (**b**) symmetry. The nomenclature of sites is detailed in Brigatti et al. (1996, 2000). Additional numbers in brackets identify the actual atom position.

experimentally recorded on randomly oriented powders on the sample-holder, in which **c*** is mostly parallel to the incident SR beam direction and the **a** and **b** axes are totally disoriented on the plane orthogonal to it, where the electric vector ε lies.

Micas with bulk compositions close to an end-member (irrespectively if phlogopite or tetra-ferriphlogopite) show XANES spectra that are sharp and well-defined (in particular feature B, and also E in the IMS energy range). Intermediate micas rich in $^{VI}Fe_{tot}$ display broad patterns, with their shoulder A, particularly, becoming less and less resolved possibly because of enhanced absorption.

Turning now to consider the dependence of the features observed in powder XANES spectra (Fig. 2a) on selected crystal-chemical and structural parameters, several observations can be formulated, as follows.

Feature C vs. neighboring O atoms. There is a well-defined trend correlating the C energy value to the tetrahedral rotation α angle (Fig. 3a), which has long been known to relate directly to ECoN (Weiss et al. 1992). This result of the statistical treatment confirms a conclusion already made, albeit more empirically (Cibin et al. 2005; Fig. 6), and points out that the energy position of feature C reflects the coordination of the basal O atoms that form the closest neighboring shell of the interlayer cation. This turns out to be even more evident when the energy variation of feature C with the variance of interlayer cation–tetrahedral basal O distances (σ A-O_{basal}) is considered (Fig. 3b). This latter parameter, together with interlayer cation-octahedral

TABLE 2. Experimental powder XANES and some structural features of trioctahedral micas relevant for this work

	phl-Fr	phl-2a	Tae23-1	Tai17-1	Tag15-4	Tag15-3	19	BHG-1	Wa8H	120	Tpq16-6	Tas22-1	47
Energy position of XANES features													
E_0	3611.5	3611.2	3611.2	3611.4	3611.3	3611.2	3611.3	3611	3611.5	3611.3	3611.5	3611	3711.2
A	3612.4	3612.2	3612.3	3612.4	3613	3612.2	3612.6	3612.2	3612.6	3612.6	3612.6	3612.2	3613.3
B	3616.2	3616.2	3616.3	3616.4	3616	3616.3	3616.4	3616.4	3616.4	3616.6	3616.4	3616.2	3616.1
C	3625.4	3624	3624.9	3625.2	3624.5	3625.1	3625.5	3625.9	3625.6	3626.6	3625.1	3624.5	3626.2
D	3630.4	3632.1	3630.9	3632.3	3631.8	3631.9	3631.5	3631.6	3631.9	3631.2	3632.5	3633	3630.5
E	3639.9	3639.6	3639.9	3639.9	3639.8	3640.1	3640.4	3640.2	3640.4	3639.2	3641	3640.7	3639.9
Geometric parameters derived from crystal-structure refinement													
α (°)	6.73	11.12	8.92	8.97	9.06	8.53	7.63	5.93	7.05	1.51	10.20	10.90	3.40
β (°)	100.08(1)	99.96(2)	99.93(3)	99.94(1)	99.99(1)	100.03(3)	100.19(1)	100.29(1)	100.15(1)	100.86(1)	100.03(2)	99.99(1)	100.73(1)
σ A-O_{basal} (Å)	0.1529	0.2512	0.2021	0.2043	0.2063	0.1939	0.1745	0.139	0.1608	0.0508	0.2339	0.2499	0.0807
A-$T_{(001)}$ (Å)	3.064(2)	3.062(3)	3.071(3)	3.081(3)	3.076(4)	3.076(4)	3.078(3)	3.087(3)	3.086(3)	3.109(3)	3.093(3)	3.093(4)	3.080(4)
σ A-T (Å)*	3.847	4.889	11.945	5.604	16.368	5.470	54.414	95.812	44.087	435.904	16.771	7.196	163.587
A-$T_{M1,(001)}$ (Å)	3.064(2)	3.063(3)	3.072(3)	3.081(3)	3.079(3)	3.076(4)	3.074(3)	3.077(3)	3.081(3)	3.056(3)	3.091(3)	3.092(4)	3.066(4)
A-$O4_{[001]}$ (Å)	4.013(2)	4.045(3)	4.030(3)	4.029(3)	4.017(4)	4.006(3)	3.988(3)	3.979(2)	3.995(3)	3.969(3)	4.038(2)	4.037(3)	3.944(3)

*$\times 10^{-4}$.

TABLE 3. Extrapolated single-crystal AXANES and relevant crystal-chemical data of trioctahedral micas

	phl-Fr	Tag 15-3	Tas 22-1	47	55	104	66
In-plane component (eV ± 0.03)							
E_0	3609.3	3611.3	3611.4	3610	3609.1	3609.5	3609.9
A	3611.9	3612.9	3612.2	3612.2	3611.1	3611.8	3612.5
B	3615.3	3618.9	3615.8	3615.3	3614.9	3614.7	3615.4
C	3624.7	3624.6	3624.8	3625	3625	3624.5	3625
D	3630.3	3631.8	3631	3630.4	3630.1	3630.4	3630.6
E	3638.4	3640.1	3639.1	3639.3	3638	3638.2	3639.2
Out-of-plane component (eV ± 0.03)							
E_0	3609.8	3610.2	3610.3	3609.8	3608.8	3609.3	3609.1
A	3611.5	3611.7	3612.2	3611	3611.5	3611.3	3611.8
B	3614.5	3615.6	3615.7	3614.3	3614.5	3614.2	3614.5
C	3621.9	3623.7	3624.-	3621.6	3621.5	3621.3	3621.5
D	3628.7		3633.-	3631.-	3628.9	3628.4	3628.9
E	3638.9	3634.3	3640.3		3639.6	3639.4	3632.2
B*		3619.3	3619.4				
Geometric parameters derived from crystal-structure refinement							
σ A-O_{basal} (Å)	0.1528	0.1939	0.2499	0.0807	0.0958	0.1102	0.0861
α (°)	6.73	8.53	10.90	3.40	3.95	4.62	3.65
A-$M1_{[001]}$ (Å)	4.997(3)	5.051(4)	5.076(3)	4.979(3)	4.952(3)	4.960(3)	4.980(4)

Note: - indicates ±1 eV error in the energy value.

anionic position distance, is again strictly related to the α angle (Fig. 4), which in turn is crystal-chemically constrained by the requirement of size-matching of the tetrahedral and octahedral sheets. Feature C is also related to the monoclinic β angle of the mica unit cell (Fig. 5a), via a non linear relationship. An approximate linear trend applies between feature C and the cosine of the monoclinic β angle, which is related in most samples to the A-O4 distance along [100] direction. However, the β and α angles are usually interrelated in micas, even though they follow trends that are different for micas with different symmetries (*C*2 and *C*2/*m*). Furthermore, feature C energy is also related to the A-O4 distance (Fig. 5b).

Feature D vs. A-$T_{(001)}$. Feature D appears to be related to the interlayer-tetrahedral sheet distances, especially when they are projected onto the (001) plane. In Figure 6, the A-$T_{(001)}$ value stands for the mean value of the interlayer cation (A)-tetrahedral cation (T) distances projected on the (001) plane. The deviation shown by samples phl-2a, 120, 47, and BHG-1 may be attributed to increased disorder in their A-$T_{(001)}$ distances, which in turn relates to their need to match the adjacent octahedral sheets, showing high Al (phl-2a) or Fe atom contents (120, 47, and BHG-1). We evaluated this possibility by using the σ A-$T_{(001)}$ parameter, which represents the variance of A-$T_{(001)}$ distances, and relating it to the $^{VI}Fe^{2+}$ total content (Fig. 7) as determined from crystal chemistry. The deviations from the trend shown by Fe^{2+}-rich micas, where annite 120 is the sample outlier, may thus be attributed to interlayer cation ordering due to the Fe^{2+} for Mg octahedral substitution, especially when the Fe^{2+} substitution is greater than 1 apfu.

In general, the A-$T_{(001)}$ distance appears to be related to several structural parameters, including the mean <T-O> distance, the *b* unit-cell parameter, and the interlayer cation–interlayer cation distances that can be expressed as a simple dependence of unit-cell parameters only.

Feature E vs. A-T distance and octahedral ordering. Feature E shows only limited variation; in some samples, it is related to feature D. It appears to relate to the distance between A and the T sites, much as feature D also does. The best-defined trends link feature E to the distance of the interlayer cation from the tetrahedral cation closer to M1 (Fig. 8), but there are some discrepancies, especially for Fe^{2+}-rich samples, in which the A-T distances shows that the T cation is closer to M2.

Single-crystal AXANES spectra

The number of processed AXANES spectra is fairly small (Table 3), but the statistical significance of their treatment is supported by the facts: (1) they were taken on trioctahedral micas already studied by the powder XANES method, and (2) span a fairly comprehensive compositional and structural set. Indeed, out of a total number of seven micas in the set that we

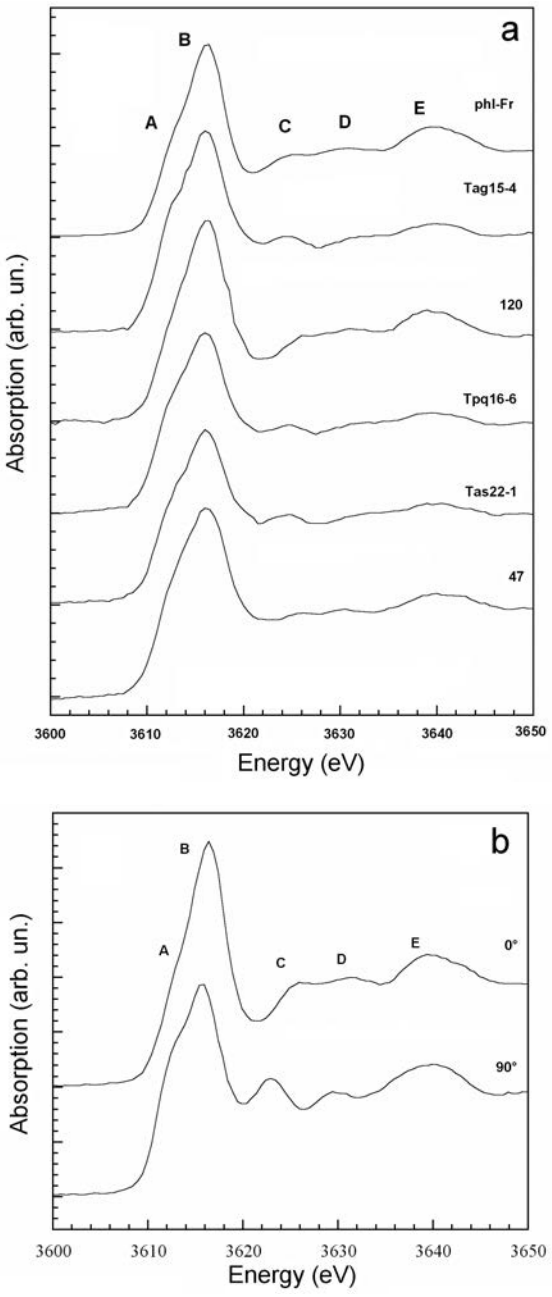

FIGURE 2. Potassium *K*-XANES spectra of some representative trioctahedral micas. (**a**) XANES powder spectra; (**b**) single-crystal AXANES spectrum at $\vartheta = 0°$ and $\vartheta = 90°$ for sample phl-Fr.

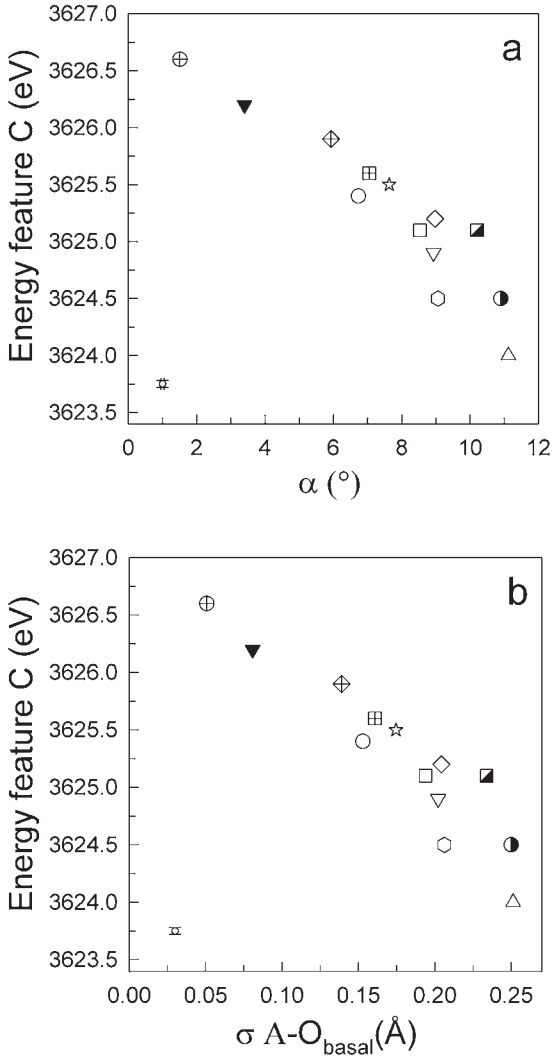

FIGURE 3. (**a**) Relationships between the energy position of spectral feature C (±0.03 eV) and the value of the tetrahedral rotation angle α. (**b**) Relationship between the energy position of spectral feature C and the variance of the distances from interlayer A cation to tetrahedral basal O atoms. Symbols: open circle = phl-Fr; open triangle up = phl-2a; open triangle down = Tae23-1; open diamond = Tai17-1; open square = Tag15-3; open hexagon = Tag15-4; open star = 19; diamond crossed = BHG1; square crossed = WAH8; filled triangle down = 47; circle crossed = 120; circle semi-filled right = Tas22-1; square semi-filled right = Tpq16-6. The relative error bar is at the lower left corner.

are now going to process statistically, two are micas belonging to the phlogopite-annite join (Tombolini et al. 2002b; Cibin et al. 2006), four are lithian micas along the polylithionite-siderophyllite join (Cibin et al. unpublished manuscript 2007), and one is a typical tetra-ferriphlogopite (Cibin et al. 2006). All these micas occur as large undeformed flakes and have potassium as their predominant A cation (Table 1[1]). Two samples, in particular, are close to end-member composition, respectively phlogopite (phl-Fr) and tetra-ferriphlogopite (Tas22-1).

These micas mainly cover the exchange vectors $^{VI}Mg_{-1}{}^{VI}Fe^{2+}$, $^{IV}Al_{-1}{}^{IV}Fe^{3+}$, and $^{IV}Si^{IV}Al_{-1}{}^{VI}Fe^{VI}Li_{-1}$. The first exchange concerns only the octahedral sheet, the second the tetrahedral sheet, and the third both sheets together. The $F_{-1}OH$ anionic exchange vector is also represented. Taken together, all these substitutions account for most of the chemical and geometric variability in the 2:1 layer of the trioctahedral subgroup of micas (Ferraris and Ivaldi 2002; Brigatti and Guggenheim 2002). The symmetry of the 2:1 layer is *C*2/*m* for all trioctahedral micas with the exception of lithian

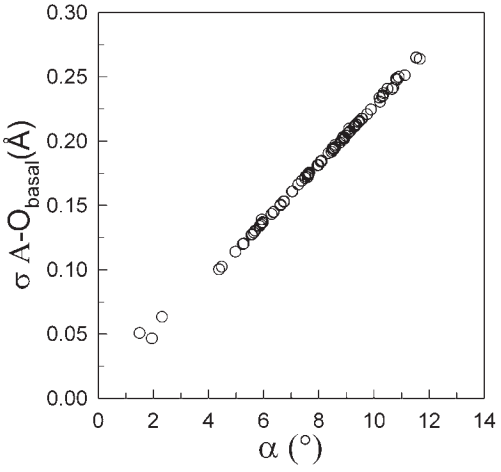

FIGURE 4. Variance of distance between interlayer cation and tetrahedral basal O atoms (σA-O_{basal}) vs. α for several mica 1*M* crystals reported in the literature.

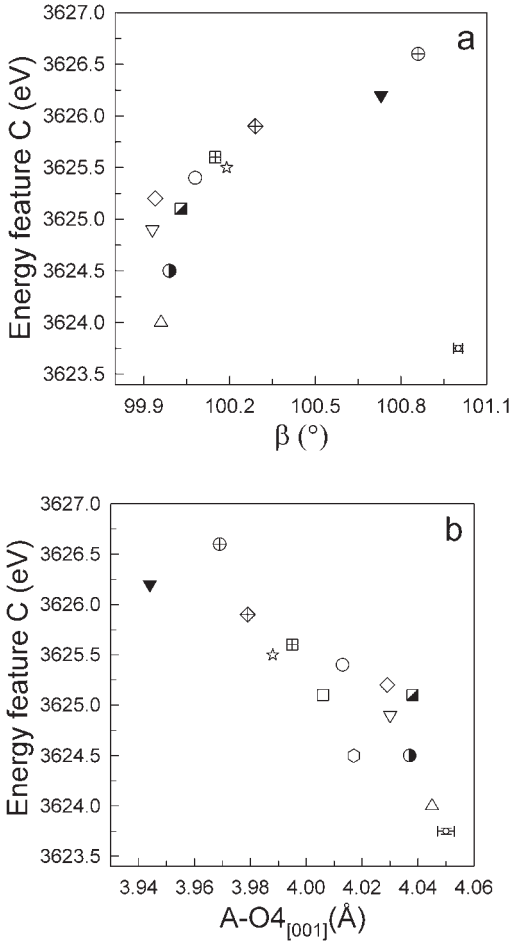

FIGURE 5. (**a**) Relationship between the energy position of spectral feature C (±0.03 eV) and monoclinic β angle. (**b**) Relationship between the energy position of spectral feature C and the projection of A-O4 distance on [001]. Symbols and samples as in Figure 3. The relative error bar is at the lower right corner.

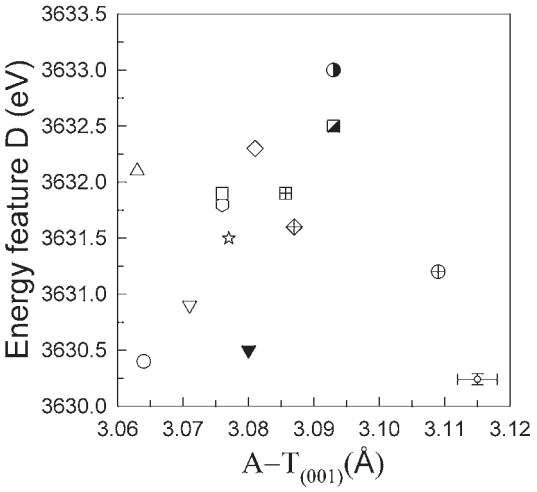

FIGURE 6. Relationship between the energy position of spectral feature D (±0.05 eV) and the projection of A-T distance on (001). Symbols and samples as in Figure 3. The relative error bar is at the lower right corner.

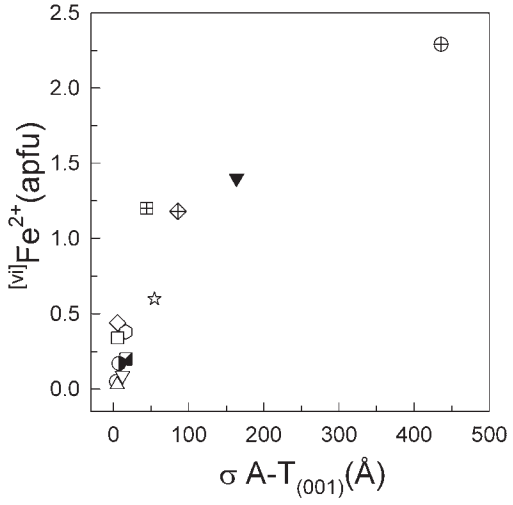

FIGURE 7. Relationship between octahedral Fe^{2+} content and the variance of the A-$T_{(001)}$ distance. Symbols and samples as in Figure 3.

micas, which are *C*2 (Table 1[1]). Thus, lithian micas have three independent M1, M2, and M3 octahedra, and layer symmetry *C*12(1), whereas the other trioctahedral micas have only two independent octahedra (M2 and M3 are symmetry related), and layer symmetry *C*12/*m*(1).

Again we studied statistically the A, B, C, D, and E features (Fig. 2b) as given by the AXANES algorithm, now for two separate groups: (1) for those extrapolated at 0° (i.e., along the plane defined by the [100] and [010] vectors), and (2) at 90° (i.e., along the direction rigorously normal to the previously defined plane). Several significant dependencies were identified.

Feature A at θ = 0°. Although limited in its energy variation, this feature appears to be negatively related to Si content. Therefore, it depends on tetrahedral substitutions (Fig. 9). Consequently, it is also correlated with many tetrahedral features,

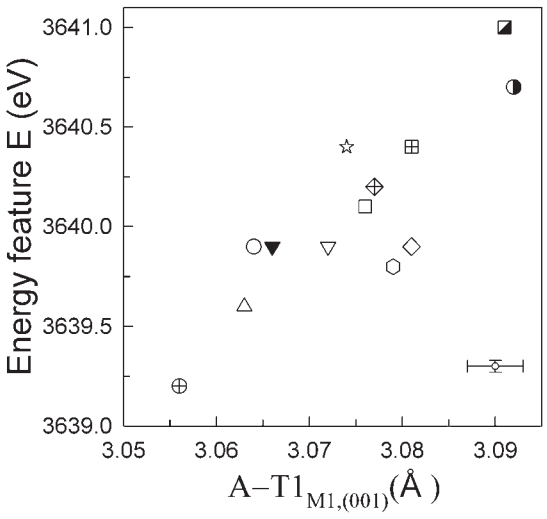

Figure 8. Relationship between the energy position of spectral feature E (±0.03 eV) and the A-T distances pertaining to M1. Symbols and samples as in Figure 3. The relative error bar is at the lower right corner.

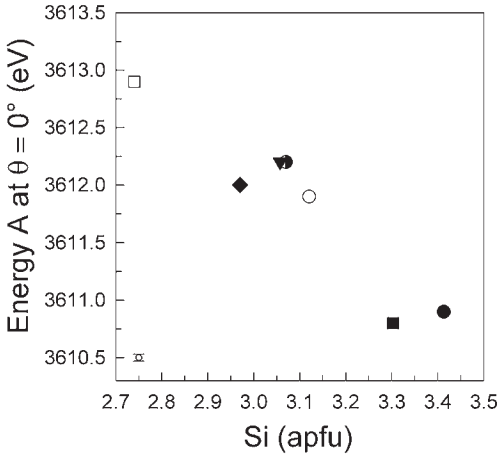

Figure 9. Relationship between the energy value of feature A at θ = 0° (±0.03 eV) and Si content. Symbols: open circle = phl-Fr; open square = Tag15-3; circle semi-filled right = Tas22-1; filled triangle down = 47; filled circle = 55; filled square = 104; filled diamond = 66. The relative error bar is at the lower left corner.

such as the A-$T_{(001)}$ distance [i.e., the interlayer cation-tetrahedral cation distance projected on (001)].

Feature A at θ = 90°. In all but one samples, this feature energy was found to be related to the variance in the A-O basal distances (Fig. 10a) and thus to the distortion of the interlayer coordination polyhedra. Consequently a well-defined correlation with the tetrahedral rotation α angle was also observed (Fig. 10b).

Feature C at θ = 90°. The energy of this feature is directly related to that of feature B at θ = 90° (Fig. 11). Both these energy features are related to the *c* unit-cell parameter and to the distance between the interlayer cation and the closest octahedral cations along the direction [001] (Fig. 12). Moreover, the energy

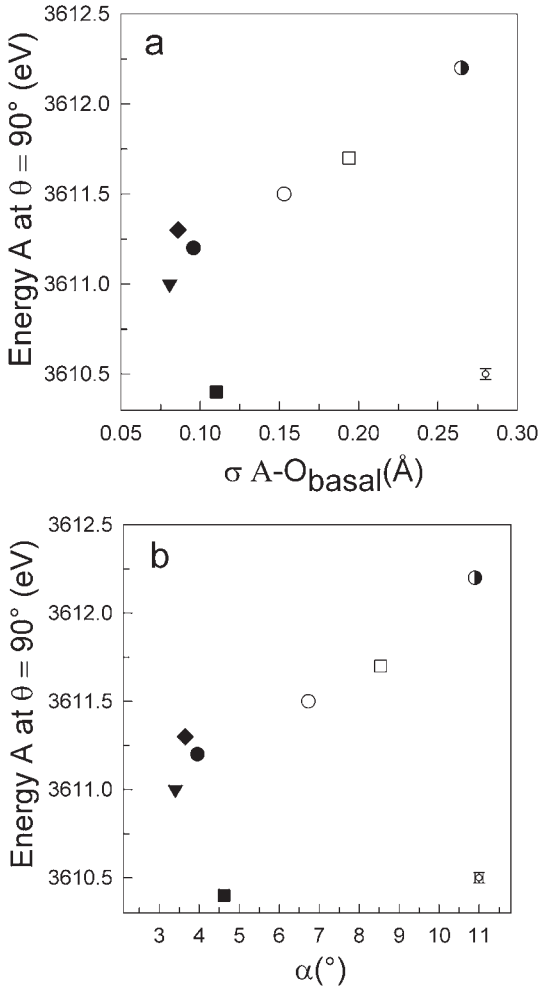

Figure 10. (**a**) Relationship between the energy value of feature A at θ = 90° (±0.03 eV) and the variance of A-O_{basal} distances. (**b**) Relationship between the energy value of feature A at θ = 90° and the tetrahedral rotation angle α. Symbols and samples as in in Figure 9. The relative error bar is at the lower right corner.

of feature C at θ = 90° seems to be affected by the octahedral anionic position and in particular by the F for OH substitution (Fig. 13).

Finally, it should also be considered that feature B* at θ = 90° (a second effect following near B at θ = 90°) appears only in samples with tetrahedral Fe content, i.e., trending to the tetra-ferriphlogopite end-member.

Discussion and concluding remarks

The following main conclusions could be drawn on powder XAFS spectra, experimentally recorded on randomly oriented powders.

(1) The energy of feature C is mostly related to the local environment around the interlayer cation (i.e., the basal O atoms of the facing tetrahedral sheets), and mostly reflects the distortion of the interlayer cation coordination.

(2) The energies of features D and E are interrelated and mostly related to the unit-cell lateral dimension *b*, and thus to

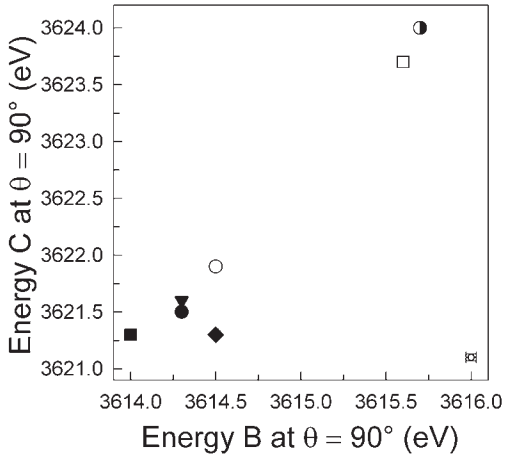

FIGURE 11. Relationship between the energy value of feature C at θ = 90° (±0.03 eV) and B at θ = 90° (±0.03 eV). Symbols and samples as in Figure 9. The relative error bar is at the lower right corner.

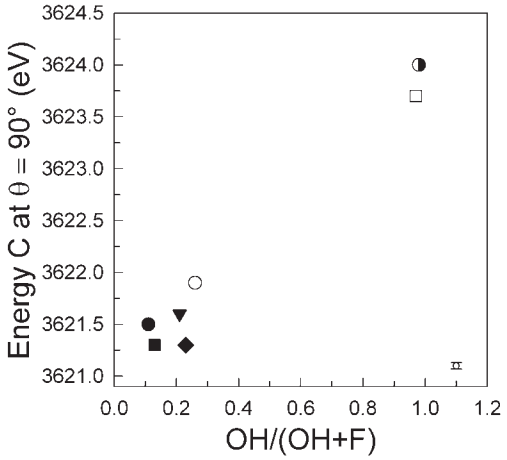

FIGURE 13. Relationship between the energy value of feature C at θ = 90° (±0.03 eV) and substitution at the O4 anionic site. Symbols and samples as in Figure 9. The relative error bar is at the lower right corner.

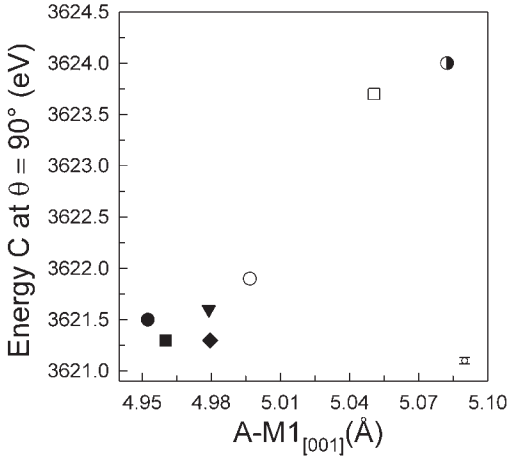

FIGURE 12. Relationship between the energy value of feature C at θ = 90° (±0.03 eV) and the distance between interlayer cation and M1 octahedral site along [001]. Symbols and samples as in Figure 9. The relative error bar is at the lower right corner.

the distances between the interlayer cation and their neighboring interlayer cations, as well as to interlayer cation–tetrahedral cation distances projected on (001): A-$T_{(001)}$.

(3) Certain samples deviate from the trends previously identified for features D and E vs. A-$T_{(001)}$. In particular, these are samples, in which the Fe^{2+} octahedral content is greater than 1 apfu, and this effect is more and more enhanced with increasing Fe content (e.g., in annite). These deviations also produce an increase in the variance of the A-$T_{(001)}$ individual distances.

(4) As a consequence of points 2 and 3, the energies of features D and E must be related to both the unit-cell lateral dimension (the distance between the interlayer cations themselves), to interlayer cation–tetrahedral cations distances along (001), and to their variance.

(5) As expected because of higher order multiple scattering contributions and/or electronic contributions, the energy positions of features A and B cannot simply associated to any structural parameters.

These conclusions on powder XAFS spectra are also supported by AXANES results.

However, feature A at θ = 90° seems to be sensitive to the same crystal chemical parameters as was feature C in powder XANES spectra, namely, to the distortion of the interlayer cation coordination. The positions of features B at θ = 90° and C at θ = 90° are related to one another and are all correlated with the F for OH substitution and to the distance between interlayer and octahedral cations along the direction [001].

The most reliable way of computing X-ray absorption spectra ab initio has been discussed over the past decades, so as making XAFS a truly quantitative method exploring the interaction pathways of the photoelectron within the probed compound. The present study fits in this frame, although it approaches the task from a completely different perspective.

We have demonstrated that the observed XANES features in mineral solid solutions can be correlated with crystal structure data. Quantitative structural and electronic information can be early extracted and confirmed by simulations performed with packages mainly based on ab initio methods and requiring several hours of computational time.

With the exception of bond distance calculations (Bianconi et al. 1983; Natoli 1984) and of pre-edge fitting (Bajt et al. 1994; Galoisy et al. 2001; Wilke et al. 2001) almost no work of this kind has been undertaken. Bugaev et al. (2001) developed a method for quantitative determination of interatomic distances and coordination number that is based on Fourier filtration of experimental XANES in the middle range order shells, followed by a fitting that is essentially an extension to the XANES energy range of the classical procedure of EXAFS fitting (Sayers et al. 1970, 1971; Lytle et al. 1974, 1975; Stern and Heald 1983). Their method works well in crystalline materials consisting of low-Z (Z < 20) atoms, because it allows the first shell distance to be

extracted together with the coordination number of the related atom, i.e., the same data determined on the EXAFS part of the XAFS spectrum. Their results are supported by our statistical relationships, and both methods suggest that the IMS region in XANES spectra is mainly reflecting the structural properties of a compound rather than the local electronic properties of the atom hosted in that compound. Tombolini et al. (2002a), as a matter of fact, could develop a method that relates the experimentally determined shift of one IMS feature in a mineral series to its composition and, by solving a set of equations, determines the average sizes of the individual tetrahedra centered by Si and Al. The method works well for micas, but so far has not been tested on other mineral families. No one, to our knowledge, ever tried relating distances determined by SC-XRD refinement to specific XANES or AXANES features.

The present study makes it now clear that certain features observed in experimental and extrapolated XANES vs. AXANES spectra statistically relate to certain atom distances, determined by SC-XRD methods that are considered to be highly reliable. Therefore, generalizing, we conclude that XAFS features reflect the existence of multiple scattering pathways of the photo-electron ejected from the absorber with nearby atoms. This result is obvious for the closest coordination shells, but it is not as obvious for the most distant shells. It was statistically shown, here, that in trioctahedral micas the photo-electron interacts not only with the atoms in the tetrahedral sheet or on the plane of the octahedral sheet closest to the interlayer, but also enters deeply in the octahedral sheet itself. The photo-electron returns to the absorber with energy and intensity features that may be related to the chemical (speciation) properties of the centro-octahedral atom encountered. In particular, the interaction with the octahedral anionic positions is related to peculiar features of XANES spectra, thus hinting at either an interaction of the emitted photo-electron with the species populating the O4 site or mirroring modifications of the interlayer topology to anionic substitutions. Only feature B (and to a lesser extent feature A), which is the closest to and the most characteristic of the *K*-edge defies correlation with structural parameters, probably predominantly reflecting the atom absorption and electronic properties rather than its being involved in the structure.

The present results open a way to calibrate the binding forces between atoms in the structure by a method that is purely based on experimental measurements, with no generic pre-requisites such as electronegativity or size. The test has been made here for K only, and needs now to be extended to other atoms such as Mg, Al, Si, and Fe, as well as to minerals other than the micas.

Acknowledgments

First of all, we are grateful to M.D. Dyar and M. Wilke, who aided as reviewers for this work, and to associate editor C.W. Elliot, for their masterly contributions to improve both readability and scientific content of this manuscript. Our research on micas enjoys the support of Italy's Ministero dell'Istruzione Università e Ricerca (MIUR) under project "Micas: cation ordering, anionic composition as petrogenetic control factors" (PRIN 2006). Spectra were recorded at Stanford Synchrotron Radiation Laboratory (SSRL), a facility operated by Stanford University and supported by U.S. Department of Energy (DOE), Office of Basic Energy Sciences, and Natural Institute of Health (NIH), Biotechnology Resource Program, Division of Research Resources. We thank the SSRL staff, particularly P. Pianetta, H. Tompkins, and C. Troxel, for advice and technical assistance. At Istituto Nazionale di Fisica Nucleare (INFN), Laboratori Nazionali di Frascati (LNF), A. Grilli and A. Raco contributed with their technical skill.

References cited

Alietti, E., Brigatti, M.F., and Poppi, L. (1995) The crystal structure and chemistry of high-aluminum phlogopite. Mineralogical Magazine, 59, 149–157.

Bajt, S., Sutton, S.R., and Delaney, J.S. (1994) Microanalysis of iron oxidation states in silicates and oxides using X-ray absorption near edge structure (XANES). Geochimica et Cosmochimica Acta, 58, 5209–5214.

Belov, N.V. (1949) The twin laws of micas and micaceous minerals. Mineralogičeski Sbornik L'vovskoho Geoločeskoho Obšestva, 3, 29–40 (in Russian).

Benfatto, M. and Della Longa, S. (2001) Geometrical fitting of experimental XANES spectra by a full multiple-scattering procedure. Journal of Synchrotron Radiation, 8, 1087–1094.

Benfatto, M., Congiu Castellano, A., Daniele, A., and Della Longa, S. (2001) MXAN: A new software procedure to perform fitting of experimental XANES spectra. Journal of Synchrotron Radiation, 8, 267–269.

Bianconi, A. (1988) XANES Spectroscopy. In D.C. Konigsberger and R. Prins, Eds., X-ray absorption: Principles, applications, techniques of EXAFS, SEXAFS, and XANES, p. 573–662. Wiley, New York.

Bianconi, A., Dell'Ariccia, M., Gargano, A., and Natoli, C.R. (1983) Bond length determination using XANES. In A. Bianconi, L. Incoccia, and S. Stipcich, Eds., EXAFS and Near Edge Structure, 27, p. 57–61. Springer Series in Chemical Physics, Springer, Berlin.

Brigatti, M.F. and Guggenheim, S. (2002) Mica crystal chemistry and the influence of pressure, temperature, and solid solution on atomistic models. In A. Mottana, F.P. Sassi, J.B. Thompson, Jr., and S. Guggenheim, Eds., Micas: Crystal Chemistry and Metamorphic Petrology, 46, p. 1–97. Reviews in Mineralogy and Geochemistry, Mineralogical Society of America, Chantilly, Virginia.

Brigatti, M.F. and Poppi, L. (1993) Crystal chemistry of Ba-rich trioctahedral micas-1*M*. European Journal of Mineralogy, 5, 857–871.

Brigatti, M.F., Medici, L., Saccani, E., and Vaccaro, C. (1996) Crystal chemistry and petrologic significance of Fe^{3+}-rich phlogopites from the Tapira carbonatite complex, Brazil. American Mineralogist, 81, 913–927.

Brigatti, M.F., Lugli, C., Poppi, L., and Elburg, M. (1998) Crystal chemistry of biotites from mafic enclaves in the Warburton granodiorite, Lachlan Fold Belt (Australia). European Journal of Mineralogy, 10, 855–864.

Brigatti, M.F., Lalonde, A.E., and Medici, L. (1999) Crystal chemistry of $^{IV}Fe^{3+}$-rich phlogopites: a combined single-crystal X-ray and Mössbauer study. Proceedings of the 11th International Clay Conference "Clays for our future," Ottawa, 1997, 317–327.

Brigatti, M.F., Lugli, C., Poppi, L., Foord, E.E., and Kile, D. (2000) Crystal chemical variations in lithium micas from the miarolitic pegmatites of the Pikes Peak batholith, central Colorado. American Mineralogist, 85, 1275–1286.

Brouder, C. (1990) Angular dependence of X-ray absorption spectra. Journal of Physics: Condensed Matter, 2, 701–738.

Brouder, C., Kappler, J.-P., and Beaurepaire, E. (1990) Theory and application of angle-resolved X-ray absorption spectra. In A. Balerna, E. Bernieri, and S. Mobilio, Eds., 2nd European Conference on Progress in X-ray Synchrotron Radiation Research Conference Proceedings, 32, 19–22.

Bugaev, L.A., Sokolenko, A.P., Dmitrienko, H.V., and Flank, A.-M. (2001) Fourier transform of XANES as a source of quantitative information of interatomic distances and coordination numbers in crystalline minerals and amorphous compounds. Physical Review B, 65, 024105-1–024105-8.

Cibin, G., Mottana, A., Marcelli, A., and Brigatti, M.F. (2005) Potassium coordination in trioctahedral micas investigated by *K*-edge XANES spectroscopy. Mineralogy and Petrology, 85, 67–87.

Cibin, G., Mottana, A., Marcelli, A., and Brigatti, M.F. (2006) Angular dependence of potassium *K*-edge XANES spectra of trioctahedral micas: Significance for the determination of the local structure of the interlayer site. American Mineralogist, 91, 1150–1162.

Ferraris, G. and Ivaldi, G. (2002) Structural features of micas. In A. Mottana, F.P. Sassi, J.B. Thompson, and S. Guggenheim, Eds., Micas: Crystal Chemistry and Metamorphic Petrology, 46, p. 117–153. Reviews in Mineralogy and Geochemistry, Mineralogical Society of America, Chantilly, Virginia.

Galoisy, L. (2004) X-ray absorption spectroscopy in geosciences: Information from the EXAFS region. In A. Beran and E. Libowitzky, Eds., Spectroscopic Methods in Mineralogy, 6, p. 553–587. European Mineralogical Union Notes in Mineralogy, Eötvös University Press, Budapest.

Galoisy, L., Calas, G., and Arrio, M.A. (2001) High-resolution XANES spectra of iron in minerals and glasses: structural information from the pre-edge region. Chemical Geology, 174, 307–319.

Hoppe, R. (1979) Effective coordination numbers (ECoN) and mean fictive ionic radii (MEFIR). Zeitschrift für Kristallographie, 150, 23–52.

Kuzmin, A. and Parent, P. (1994) Focusing and superfocusing effects in X-ray absorption fine structure at the iron *K* edge in FeF_3. Journal de Physique: Condensed Matter, 6, 4395–4404.

Lee, H.-L. and Guggenheim, S. (1981) Single crystal refinement of pyrophyllite-1*Tc*. American Mineralogist, 66, 350–357.

Lytle, F.W., Sayers, D.E., and Stern, E.A. (1974) Structure of catalysts: Determination by EPR and Fourier analysis of the extended X-ray absorption fine structure. Applied Physics Letters, 24, 45–47.

Lytle, F.W., Sayers, D.E., and Stern, E.A. (1975) Extended X-ray-absorption fine-structure technique. II. Experimental practice and selected results. Physical Review, B11, 4825–4835.

Marcelli, A., Cibin, G., Cinque, G., Mottana, A., and Brigatti, M.F. (2006) Polarized XANES spectroscopy: the *K*-edge of layered K-rich silicates. Radiation Physics and Chemistry, 75, 1596–1607.

Mottana, A. (2004) X-ray absorption spectroscopy in mineralogy: Theory and experiment in the XANES region. In A. Beran and E. Libowitzky, Eds., Spectroscopic Methods in Mineralogy, 6, p. 465–522. European Mineralogical Union Notes in Mineralogy, Eötvös University Press, Budapest.

Mottana, A., Marcelli, A., Cibin, G., and Dyar, M.D. (2002) X-ray absorption spectroscopy of the micas. In A. Mottana, F.P. Sassi, J.B. Thompson, and S. Guggenheim, Eds., Micas: Crystal Chemistry and Metamorphic Petrology, 46, p. 371–412. Reviews in Mineralogy and Geochemistry, Mineralogical Society of America, Chantilly, Virginia.

Natoli, C.R. (1984) Distance dependence of continuum and bound state of excitonic resonance in X-ray absorption near-edge structure (XANES). In K.O. Hodgson, B. Hedman, and J.E. Penner-Hahn, Eds., EXAFS and Near-Edge Structure III, p. 38–42. Springer, Berlin.

Natoli, C.R. and Benfatto, M. (1986) A unifying scheme of interpretation of X-ray absorption spectra based on the multiple scattering theory. In P. Lagarde, D. Raoux, and J. Petiau, Eds., EXAFS and Near Edge Structure IV. Journal de Physique, 47–Colloque 8, 11–23.

Natoli, C.R., Benfatto, M., Della Longa, S., and Hatada, K. (2003) X-ray absorption spectroscopy: state-of-the-art analysis. Journal of Synchrotron Radiation, 10, 26–42.

Pauling, L. (1930) The structure of micas and related minerals. Proceedings of the National Academy of Science (USA), 16, 123–129.

Radoslovich, E.W. (1961) Surface symmetry and cell dimensions of layer-lattice silicates. Nature, 191, 67–68.

Radoslovich, E.W. and Norrish, K. (1962) The cell dimensions and symmetry of layer-lattice silicates. I. Some structural considerations. American Mineralogist, 47, 599–616.

Sayers, D.E., Lytle, F.W., and Stern, E.A. (1970) Point scattering theory of X-ray K-absorption fine structure. In B.L. Henke, J.B. Newkirk, and G.R.Mallett, Eds., Advances in X-ray Analysis, 13, p. 248–271. Plenum, London.

Sayers, D.E., Stern, E.A., and Lytle, F.W. (1971) New technique for investigating noncrystalline structures: Fourier analysis of the extended X-ray absorption fine structure. Physical Review Letters, 27, 1204–1208.

Schingaro, E., Scordari, F., Mesto, E., Brigatti, M.F., and Pedrazzi, G. (2005) Cation-site partitioning in Ti-rich micas from Black Hill (Australia): A multi-technical approach. Clays and Clay Minerals, 53, 179–189.

Smyth, J.R. and Bish, D.L. (1988) Crystal structures and cation sites of rock-forming minerals. Allen and Unwin, Boston.

Stern, E.A. and Heald, S.M. (1983) Basic principles and applications of EXAFS. In E.E. Koch, Ed., Handbook on Synchrotron Radiation. V. 1b, p. 955–1014. North-Holland, New York.

Takéuchi, Y. and Sadanaga, R. (1959) The crystal structure of xanthophyllite. Acta Crystallographica, 12, 945–946.

Tombolini, F., Brigatti, M.F., Marcelli, A., Cibin, G., Mottana, A., and Giuli, G. (2002a) Local and average Fe distribution in trioctahedral micas: Analysis of the Fe *K*-edge XANES spectra in the phlogopite-annite and phlogopite-tetraferriphlogopite joins on the basis of single-crystal XRD refinements. European Journal of Mineralogy, 14, 1075–1186.

Tombolini, F., Marcelli, A., Mottana, A., Cibin, G., Brigatti, M.F., and Giuli, G. (2002b) Crystal-chemical study by XANES of trioctahedral micas: The most characteristic layer silicates. International Journal of Modern Physics, B16, 1673–1679.

Weiss, Z., Rieder, M., and Chmielová, M. (1992) Deformation of coordination polyhedra and their sheets in phyllosilicates. European Journal of Mineralogy, 4, 665–682.

Wilke, M., Farges, F., Petit, P.-E., Brown, G.E., Jr., and Martin, F. (2001) Oxidation state and coordination of Fe in minerals: An Fe *K*-XANES spectroscopic study. American Mineralogist, 86, 714–730.

Manuscript received March 20, 2007
Manuscript accepted December 28, 2007
Manuscript handled by W. Crawford Elliott